Comparing turbulence in a Kelvin–Helmholtz instability region across the terrestrial magnetopause

Paulina Quijia, Federico Fraternale, Julia E Stawarz, Christian L Vásconez, Silvia Perri, Raffaele Marino, Emiliya Yordanova, Luca Sorriso-Valvo

Monthly Notices of the ROYAL ASTRONOMICAL SOCIETY

MNRAS **503,** 4815–4827 (2021) doi:10.1093/mnras/stab319
Advance Access publication 2021 February 5

Comparing turbulence in a Kelvin–Helmholtz instability region across the terrestrial magnetopause

Paulina Quijia,[1,2] Federico Fraternale,[3] Julia E. Stawarz,[4] Christian L. Vásconez ,[2] Silvia Perri,[1] Raffaele Marino,[5] Emiliya Yordanova[6] and Luca Sorriso-Valvo [6,7]★

[1]*Dipartamento di Fisica, Università della Calabria, ponte P. Bucci, cubo 31C, I-87036 Rende, Italy*
[2]*Departamento de Física, Escuela Politécnica Nacional, Av. Ladrón de Guevara E11-253, 170525 Quito, Ecuador*
[3]*Center for Space Plasma and Aeronomic Research, The University of Alabama in Huntsville, Huntsville, AL 35805, USA*
[4]*Department of Physics, Imperial College London, SW7 2BU London, UK*
[5]*Laboratoire de Mécanique des Fluides et d'Acoustique, CNRS, École Centrale de Lyon, Université Claude Bernard Lyon 1, INSA de Lyon, F-69134 Écully, France*
[6]*Swedish Institute of Space Physics, SE-751 21 Uppsala, Sweden*
[7]*CNR – Istituto per la Scienza e Tecnologia dei Plasmi, via Amendola 122/D, I-70126 Bari, Italy*

Accepted 2021 February 1. Received 2021 February 1; in original form 2020 December 31

ABSTRACT

The properties of turbulence observed within the plasma originating from the magnetosheath and the magnetospheric boundary layer, which have been entrained within vortices driven by the Kelvin–Helmholtz Instability (KHI), are compared. The goal of such a study is to determine similarities and differences between the two different regions. In particular, we study spectra, intermittency and the third-order moment scaling, as well as the distribution of a local energy transfer rate proxy. The analysis is performed using the Magnetospheric Multiscale data from a single satellite that crosses longitudinally the KHI. Two sets of regions, one set containing predominantly magnetosheath plasma and the other containing predominantly magnetospheric plasma, are analysed separately, thus allowing us to explore turbulence properties in two portions of very different plasma samples. Results show that the dynamics in the two regions is different, with the boundary layer plasma presenting a shallower spectra and larger energy transfer rate, indicating an early stage of turbulence. In both regions, the effect of the KHI is evidenced.

Key words: MHD – plasmas – turbulence – solar wind.

1 INTRODUCTION

Understanding the basic processes of astrophysical plasmas relies strongly on the *in-situ* experimental study of space plasmas. The fleet of past and present satellites, equipped with tailored payloads, provide a large amount of observations of plasma and electromagnetic fields in various regions of the Solar System, from the inner heliosphere to the local interstellar medium. One of the most defining features of heliospheric plasma is turbulence. Highly chaotic plasma and fields fluctuations, originated by a non-linear energy cascade (Biskamp 1993; Frisch 1995), are indeed seen in the solar photosphere and corona, in the solar wind, in the planetary magnetospheres, and in most of the structures therein (Petrovay 2001; Saur, Politano & Pouquet 2002; Chandran 2005; Uritsky, Paczuski & Davila 2007; Bruno & Carbone 2013; Von Papen, Saur & Alexandrova 2014). Understanding the properties of turbulence and the associated physical processes is fundamental for the correct description of space plasma dynamics, and consequently for the correct interpretation of astrophysical observations (Cho, Lazarian & Vishniac 2003). For this reason, theoretical, experimental, and numerical studies have largely been carried out in the last decades, producing important, yet incomplete, advances towards a satisfactory description of heliospheric plasma turbulence (Bruno & Carbone 2013). In this perspective, the terrestrial magnetosphere represents the ideal environment for experimental studies of the processes occurring in the proximity of plasma boundaries, such as the terrestrial bow-shock and magnetopause, separating the interplanetary medium from the magnetospheric plasma. Turbulence properties can help in understanding the mechanisms of interaction between the solar wind and the magnetosphere, as for example the transport of mass, momentum, and energy (Zimbardo et al. 2008; Pucci et al. 2016). Previous studies have shown that the turbulent solar wind is heavily processed by the bow shock, so that in the magnetosheath a Kolmogorov turbulent spectrum only develops away from the shock (Breuillard et al. 2018; Macek et al. 2018; Yordanova et al. 2020). On the other hand, in the magnetospheric boundary layer region the plasma is only weakly turbulent, being characterized by smaller fluctuations and reduced bulk motion (Treumann 1999; Hasegawa et al. 2019).

In the last decade the launch of the Magnetospheric Multiscale (MMS) mission has allowed a great advance in the knowledge of the turbulent cascade at intermediate scales, and of the kinetic process at subproton scales in the near-Earth environment, thanks to the very high resolution reached both in the magnetic field measurements, and in the plasma data. Processes such as the interaction between particle and turbulent fluctuations or small-scale reconnection, both close to the ion inertial scale and to the electron inertial scale, have

★ E-mail: lucasorriso@gmail.com

been studied in depth, shedding light on the plasma dissipation mechanisms (Burch et al. 2016; Vörös et al. 2016; Yordanova et al. 2016; Eriksson et al. 2016b; Perri et al. 2020).

Among the most studied phenomena related to turbulence, the Kelvin–Helmholtz Instability (KHI) is occasionally observed to take place at the magnetopause. Kelvin–Helmholtz waves develop at the terrestrial magnetopause, where small-scale perturbations may gain energy from the velocity shear between the magnetospheric and magnetosheath plasma, growing into large-scale rolled up vortices (Sundberg et al. 2012). When the instability grows to reach a turbulent state, plasma and energy can be transported from the dense magnetosheath into the more rarefied magnetosphere (Mitchell et al. 1987; Bavassano Cattaneo et al. 2010; Johnson, Wing & Delamere 2014; Nakamura et al. 2017a). The KHI can also drive the turbulence in the magnetosheath region, acting as a large-scale mechanism which initiates or reinforces a non-linear cascade (Chen et al. 1993; Kokubun et al. 1994; Fairfield et al. 2000, 2003, 2007; Otto & Fairfield 2000; Hasegawa et al. 2004; Karimabadi et al. 2013). Observations suggest the presence of Kelvin–Helmholtz waves on both the dawn and dusk flank of the terrestrial magnetosphere (Chen et al. 1993; Kokubun et al. 1994; Fairfield et al. 2000, 2007; Otto & Fairfield 2000; Farrugia et al. 2001; Fujimoto, Tonooka & Mukai 2003; Hasegawa et al. 2004; Stawarz et al. 2016). Studying a KHI region can help with understanding the role of the instability in determining or modifying the characteristics of turbulence, such as scale-invariance and intermittency. To this aim, we analysed in depth the statistical properties of the turbulence present in the magnetosheath-origin and boundary-layer-origin plasma that is entrained within the Kelvin–Helmholtz vortices, observed by the payload onboard MMS while crossing the transition between the magnetosheath and the magnetospheric boundary layer (Eriksson et al. 2016a; Stawarz et al. 2016; Sorriso-Valvo et al. 2019a; Franci et al. 2020).

The article is organized as follows. In Section 2, we describe the data set and the procedure to separate the two distinct regions of plasma. Sections 3 and 4 present the results of the standard analysis of turbulence, such as autocorrelation functions, spectra, and structure functions. In Section 5, the scaling properties of the global energy transfer rate are studied, both in the magnetohydrodynamic and Hall–magnetohydrodynamic approximation. Section 6 focuses on the statistical properties of a local proxy for the local turbulent energy transfer rate. Finally, comparisons and conclusions are drawn in Section 7.

2 MAGNETOSPHERIC MULTISPACECRAFT MISSION DATA

In order to study the differences in the turbulence properties between magnetospheric boundary layer and magnetosheath origin plasma within a Kelvin–Helmholtz instability, we use measurements from the MMS mission (Burch et al. 2016). The MMS high-cadence ion (150 ms) (Pollock et al. 2016) and magnetic field (128 Hz) (Russell et al. 2016) measurements provide a rich data base for performing a statistical analysis. The selected data interval was measured by MMS on 2015 September 8 from 10:07:04 UT to 11:25:34 UT in the dusk-side magnetopause. During this period, the spacecraft traversed from the low-latitude boundary layer (BL) into the magnetosheath (MS), experiencing many crossings of the large-scale vortices generated by the KHI. Crossings were detected as ion-scale periodic current sheets (Eriksson et al. 2016b), separating the more rarefied and hotter magnetospheric plasma from the denser and colder magnetosheath. Fig. 1 provides an overview of plasma and fields parameters for one example of several of the vortex crossings within the event.

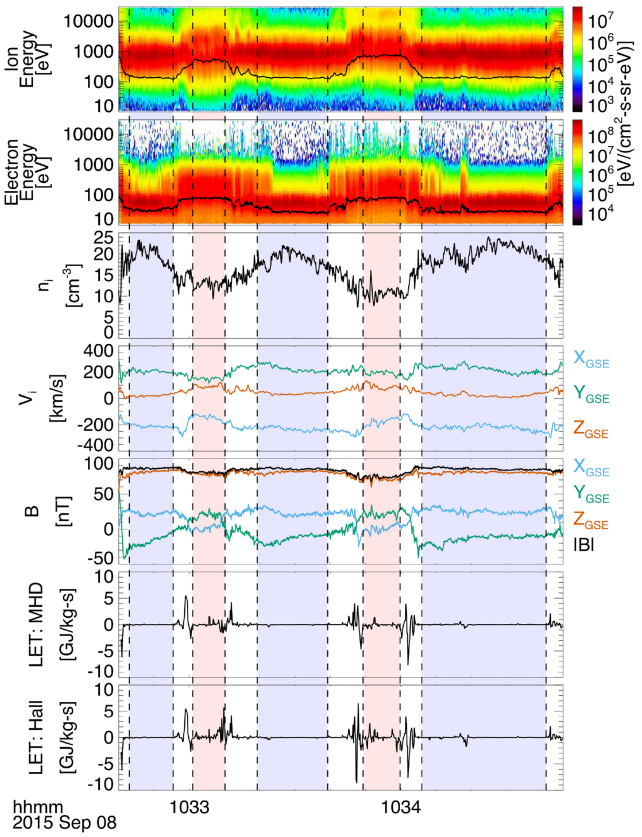

Figure 1. An example of the intervals used for this work. A fraction of the entire event is shown, in this case spanning from 10:32 to 10:35 UTC on 2015 September 8. From top to bottom: ion energy distribution and temperature (black line); electron energy distribution and temperature (black line); ion density; ion velocity components; magnetic field components and magnitude; the MHD LET; the Hall–MHD LET. The velocity and magnetic vectors are given in the GSE system. The red and blue shaded areas indicate examples of the selected sub-intervals in the boundary layer and in the magnetosheath, respectively.

All vectors are presented in the standard GSE coordinate system. The ion velocity and density, together with the magnetic field re-sampled at the same cadence (150 ms), were used for this analysis. The current density has been computed as $\mathbf{J} = nq(\mathbf{V}_i - \mathbf{V}_e)$, with $n = n_i \sim n_e$ being the plasma density, and $\mathbf{V}_i$ and $\mathbf{V}_e$ the ion and the electron velocities, respectively. Previous studies have shown that this interval was characterized by turbulence, with a traditional power-law Kolmogorov spectrum in the fluid range of scales, followed by a steeper decay at ion scales (Stawarz et al. 2016; Sorriso-Valvo et al. 2019a). Intermittency (Stawarz et al. 2016; Franci et al. 2020) and the third-order moment scaling laws were also studied in different subsets of the interval (Sorriso-Valvo et al. 2019a; Franci et al. 2020), but a direct comparison between the two regions was never performed.

In order to identify, and separate, the MS and the BL regions, and to perform a statistical analysis on each, the selection criteria used to extract sub-intervals were the following: (i) sub-intervals composed entirely of MS or BL origin plasma, as estimated using temperature thresholds ($T_{MS} > 400$ eV, $T_{BL} < 250$ eV); (ii) approximate stationarity and homogeneity; (iii) absence of large discontinuities and boundary crossings; (iv) duration of at least 10 s (see in next section an estimate of the correlation time-scale); (iv) absence of data gaps. With these conditions, we ended up with two ensembles

Table 1. Average plasma parameters and typical scales for the BL and MS subsets: magnetic field magnitude B (nT), bulk flow speed U (km s^{-1}), perpendicular bulk flow speed $U_\perp$ (km s^{-1}), Alfvén speed V_A (km s^{-1}), ion sound speed $C_{s,i}$ (km s^{-1}), ion number density n (cm^{-3}), perpendicular ion temperature $T_\perp$ (eV), perpendicular ion beta β_i, ion Larmor radius ρ_i (km), electron Larmor radius ρ_e (km), ion inertial length r_i (km), ion plasma frequency f_{pi} (Hz), electron plasma frequency f_{pe} (Hz), ion cyclotron frequency f_{ci} (Hz), electron cyclotron frequency f_{ce} (Hz), Doppler-shifted ion cyclotron frequency $f_{ci,\,sc}$ (Hz), and Doppler-shifted ion inertial scale $f_{i,\,sc}$ (Hz). In all occurrences, perpendicular is to be intended with respect to the magnetic field.

Parameter	BL	MS
B	72.4	79.9
U	203.1	268.3
$U_\perp$	184	250
V_A	501	453
$C_{s,i}$	341	201
n	10.5	15.4
$T_\perp$	767	265
β_i	0.58	0.25
ρ_i	38.6	20.6
ρ_e	0.9	0.48
r_i	70.5	58.3
f_{pi}	680	820
f_{pe}	2.9×10^4	3.4×10^4
f_{ci}	1.10	1.22
f_{ce}	2.0×10^3	2.2×10^3
$f_{ci,\,sc}$	0.7	1.9
$f_{i,\,sc}$	0.4	0.68

of 59 MS sub-intervals, having an average length of 2.35 min, and of 24 BL ones with 0.63 min average-time length. Several of the sub-intervals are highlighted as red (BL) and blue (MS) shaded regions in Fig. 1. While these selection criteria separate out regions within the vortices containing predominantly MS or BL origin plasma, all of these sub-intervals consist of plasma that is entrained within the KHI. Therefore, these regions may have fluctuation properties that are different from the 'pristine' MS and BL plasma that is not entrained within the vortices through the action of processes that are initiated by the KHI such as plasma mixing, vortex-induced magnetic reconnection, and secondary instabilities. The goal of this study is to explore how the turbulence within these two sub-regions of the vortices differ from each other as the KHI is in the process of developing.

For the two sets (BL and MS evaluated separately), some relevant parameters are listed in Table 1 (see table caption for the relevant units). With the observed values of the Alfvén speed, the Taylor's hypothesis is adopted to estimate perpendicular wavenumbers $k_\perp \approx 2\pi/U_\perp$ (U is the bulk speed and the subscripts $\perp$ and $\shortparallel$ indicate the component perpendicular and parallel to the mean magnetic field, respectively) under the assumption of $k_\perp \gg k_\shortparallel$, as done in previous studies (Stawarz et al. 2016; Sorriso-Valvo et al. 2019a). The cyclotron scales are then Doppler-shifted to the spacecraft frame.

In order to verify the correct separation of the MMS interval in two homogeneous ensembles, Fig. 2 shows examples of the histograms of one velocity component (v_x) and ion temperature, estimated for the whole data interval (KHI, grey area), for the BL sub-intervals (red area), and for the MS sub-intervals (blue area). After separation, for each of the two ensembles, the distributions are roughly Gaussian (black-solid lines in the figure indicate Gaussian fits), suggesting that the separation has effectively collected homogeneous plasma samples. Conversely, the whole interval can be roughly fitted to

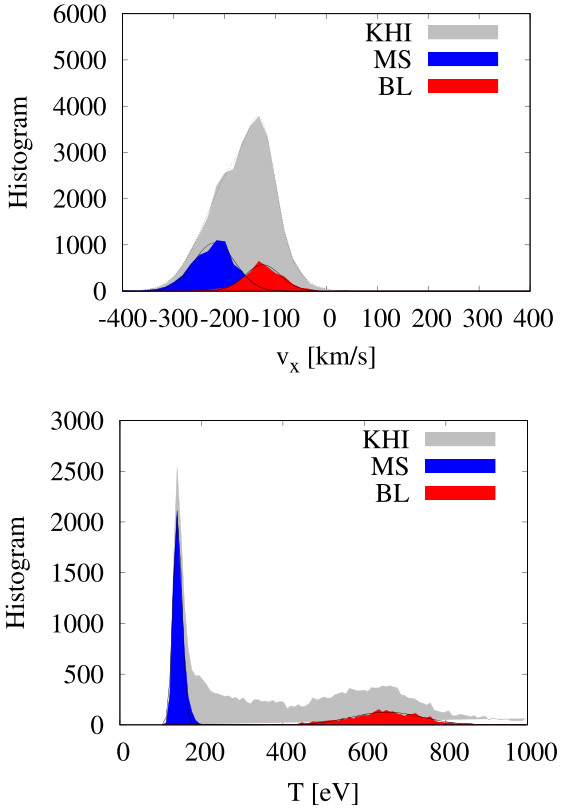

Figure 2. Histograms of the velocity component, v_x (top panel), and of the ion temperature (bottom panel). Grey area: the whole interval (KHI); red area: the boundary layer intervals (BL); blue area: the magnetosheath intervals (MS). The black full lines indicate Gaussian fits for the two sub-regions, while the black dotted line are double-Gaussian fits for the whole interval (note that double-Gaussian fit was not possible for the temperature).

a double-Gaussian (black-dotted line). Similar plots for all the components of velocity, magnetic field, current density, and for ion density (not shown) reveal similar behaviour as for v_x. From this figure, it is evident that the ion temperature is the best parameter to separate the two ensembles, since the two populations are clearly completely separated.

3 SPECTRAL PROPERTIES OF TURBULENCE

The basic indicators of a turbulent cascade are obtained through the analysis of the scaling properties of the fields. The autocorrelation function and, equivalently, the power spectral density of the turbulent fluctuations provide first-order estimates of the scaling properties of the system (Bruno & Carbone 2013). Additional information on the inhomogeneity and efficiency of the turbulent cascade, i.e. on intermittency, is provided by the anomalous scaling of the statistical properties of the field increments. In this section, the standard estimators of the above properties are presented, and compared, for the two regions described in Section 2.

As described in the previous section, each continuous sub-interval composing the two ensembles can be as short as 10 s, with average length of the order of a few minutes. This makes the evaluation of the spectral properties challenging, particularly for periods larger than, or of the order of, minutes. To overcome this issue, two different spectral estimators are used, and compared, to investigate the two regions separately. Results of the analysis are collected in Figs 3

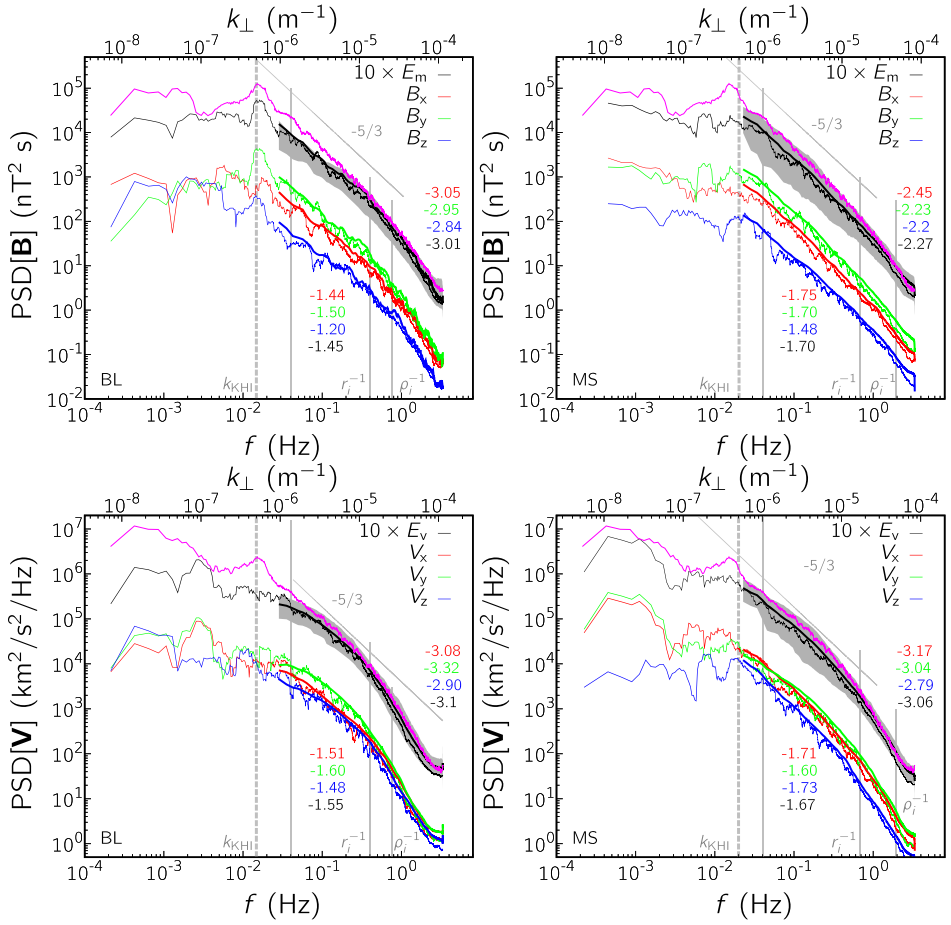

Figure 3. Magnetic field (top) and velocity (bottom) power spectra computed in the BL side (left-hand panel) and in the MS side (right-hand panel). Thick curves show the averaged spectrum obtained from the ensemble of sub-samples (method SS), while thin curves show the spectrum obtained from compressed sensing algorithm (CS). The magenta curves show the spectral trace of the full KHI time-series, shifted by a factor of 10, and refer to the frequency axis only. The spectral index is computed from power-law fit in the log–log plane in the two frequency ranges: $f \in [0.04, 0.5]$ Hz, and $f \in [1, 2.5]$ Hz for the magnetic field, and $f \in [0.04, 0.4]$, and $f \in [0.6, 1.5]$ Hz for the velocity. The average value from methods CS and SS is displayed for each component and the trace. The estimated uncertainty, which includes both the fit uncertainty and the difference between the two techniques, is below 0.05 for the magnetic field, and less than 0.06, and 0.03 in the two regimes, respectively, for the velocity. Two grey vertical lines in all panels indicate the ion inertial scale, r_i and the ion Larmor scale, ρ_i. Note that the PSD units are different for velocity and magnetic field, so that comparison of the amplitudes is not possible in this plot.

and 4, which display the power spectral density (PSD) of magnetic, velocity, and Elsasser fields, $\mathbf{z}^{\pm} = \mathbf{v} \pm \mathbf{B}/\sqrt{\mu_0 m_p n_p}$, for the MS and BL intervals, respectively. The typical scales, averaged over the whole sets, are indicated by vertical lines. In all panels of Fig. 3, we also show the frequency spectrum obtained from the complete KHI time-series (magenta curves). The first technique computes the averaged spectrum from the ensemble of individual subsets (SS, see the thick curves in the figures). The Hann window is used to reduce spectral leakage at high frequencies. The lowest frequency observed is of the order of 0.01–0.03 Hz. The second technique utilizes the compressed sensing (CS), a novel paradigm designed for sparse data (Candes, Romberg & Tao 2006; Donoho 2006). We already demonstrated the applicability of CS to solar wind, heliosheath, and interstellar Voyager data sets with up to 75 per cent of missing data (Gallana et al. 2016; Fraternale et al. 2019a, b; Fraternale, Pogorelov & Burlaga 2020), and also for MMS data (Sorriso-Valvo et al. 2019a). Here, its capability to recover non-uniformly sampled data is fully exploited to estimate the spectrum of the MS sub-intervals only and, separately, of the BL sub-intervals only, after masking the non-relevant portions of the full KHI sequence. This technique allows the spectrum to extend towards lower frequencies then the range detectable by SS, reaching frequencies as low as 10^{-4} Hz. Moreover, spectral leakage is reduced for high frequencies near the Nyquist's. The full range is indeed visible in Figs 3 and Fig. 4, where the CS spectra are represented by thinner lines. In the inertial and kinetic ranges, the two techniques give identical results, within a ~ 3.5 per cent discrepancy on the spectral index in the inertial regime where CS return slightly smaller values. In the kinetic regime, the difference reduces to 1.2 per cent. However, the access to low frequencies through the CS technique provides substantial new information.

From a look at the spectral power amplitudes, and corroborated by quantitative estimates, the following differences can be identified between MS and BL.

The magnetic field variance computed from detrended data is about 220 nT^2 in the BL, and ~ 24 per cent less in the MS. The variance of the velocity field is about 5540 km^2 s^{-2} in the BL and 5 per cent larger in the MS. This difference is due to the large-scale fluctuations below the KH frequency. At higher frequencies, the spectral density is slightly larger in the BL. Note that the PSD

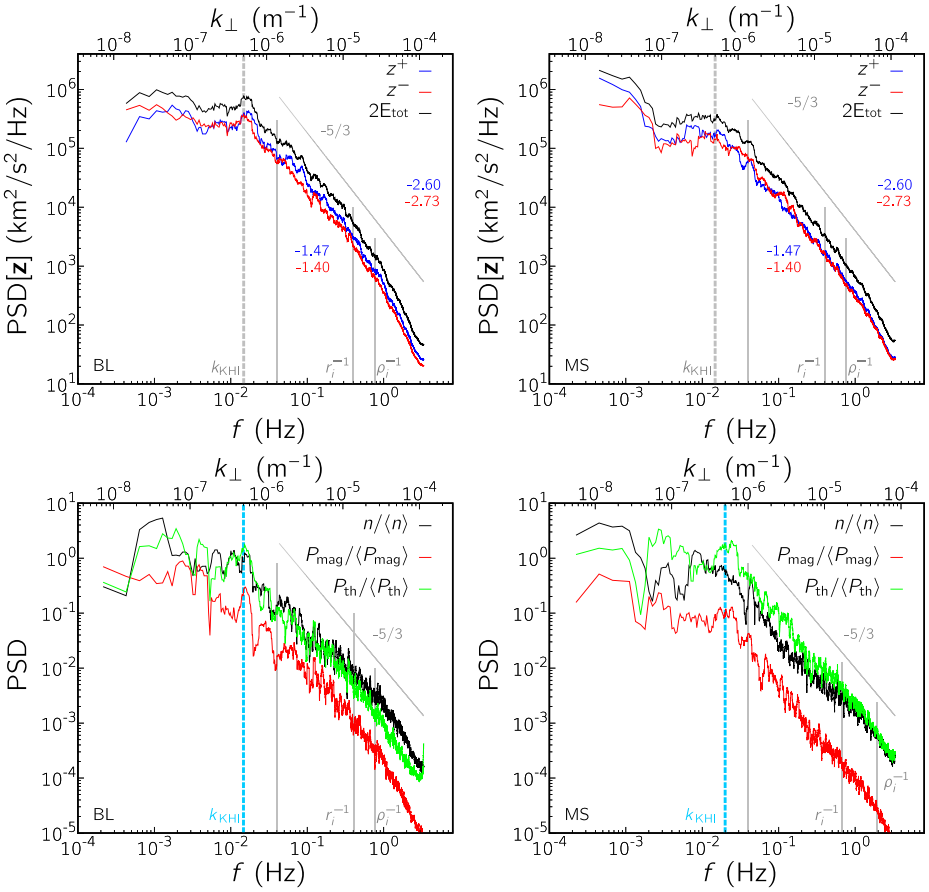

Figure 4. Top panels: trace of the power spectral density of the Elsasser field $\mathbf{z}^{\pm}$ (red and blue curves) and total energy (black curves). The spectral indexes reported in the panels are computed for the same frequency ranges of Fig. 3. Bottom panels: Power spectra of ion density n (black), magnetic pressure $P_{\rm mag}$ (red), and thermal pressure $P_{\rm th}$ (green), normalized to the respective average value. Bottom left-hand panel: BL. Bottom right-hand panel: MS.

units are different for velocity and magnetic field, so amplitudes cannot be directly compared in Fig. 3. Variances of the Elsasser fields are larger in the BL due to the effect of density fluctuations, about 25 900 and 20 820 km^2 s^{-2} for z^+ and z^-, respectively. They reduce by 45 per cent and 33 per cent in the MS.

In the low-frequency range, the magnetic power spectra show a clear peak located at or near the KHI period of 63.3 s, as estimated by Eriksson et al. (2016a). The peak is particularly visible at $f_{\rm KH} = 1.58 \times 10^{-2}$ Hz in the BL side (Fig. 3, left-hand panel), while it is not evident in the MS. Under the Taylor's approximation, we obtain from BL the perpendicular wavenumber of $k_{\perp,\,\rm KH} \approx 5 \times 10^{-7}$ m^{-1}, which is shown by blue vertical lines in all panels of these figures. This shows that, in terms of wavenumbers, the peaks in MS and BL spectra are in good agreement. At lower frequency, both regions have generally irregular but rather flat spectra, a feature that had been observed before in the MS (Breuillard et al. 2018; Macek et al. 2018; Yordanova et al. 2020) and in the BL (Hasegawa et al. 2019). This is generally attributed to the decorrelation of the fluctuations occurring at the bow-shock and at KHI, and to the limited time available for non-linear interactions to form a broad, fully developed Kolmogorov spectrum (Huang et al. 2017; Stawarz et al. 2019). Some features, likely sub-harmonics and harmonics of the KH instability, may also be noticed. A first spectral bump is centred on the frequency of 4.5×10^{-4} Hz. This is particularly evident in the density and in the MS velocity filed. A second major bump exists near the frequency of 2.5×10^{-3} Hz. In the BL, the magnetic field spectrum clearly shows regular oscillations until the frequency of 10^{-1} Hz. In the MS, the velocity power seems to become dominating with respect to the magnetic field (compare Figs 4 and 3), and display an overall slight increase towards smaller scales. This could be due to the stronger velocity shear normally driving the KH instability (Lu et al. 2019).

The CS method has therefore allowed a detailed low-frequency spectral analysis, confirming its effectiveness in dealing with incomplete data or when, as in this case, data removal is required to ensure sample homogeneity.

At intermediate frequency, the presence of a power-law range with spectral index compatible with the standard turbulence is evident for all components and for the total turbulent energy (E_m, E_v) of both fields in both regions, suggesting the existence of a turbulent inertial range (Bruno & Carbone 2013). In all cases, a spectral break located in the proximity of the proton scales is followed by a possible power-law scaling, with steeper index, typical of kinetic-scale fluctuations (Alexandrova et al. 2008). All scaling exponents are indicated and colour-coded inside each panel. The power-law scaling in the inertial range is observed on a wider range and better defined in the MS than in the BL, in particular for the velocity components and magnitude. This is also evident from the spectral trace of the Elsasser field shown in Fig. 4. The spectral index is generally closer to the Kolmogorov's $-5/3$ in the MS intervals, while it is around $-3/2$ in the BL, for scales between the driving instability and the ion inertial length. Previous observations of magnetic spectra

in the BL showed the presence of power-law scaling, with similar exponents, only in the presence of KHI (Treumann 1999; Hasegawa et al. 2019). This suggests that while the early-stage turbulence in the BL is mostly being locally driven by the KHI, in the MS there is pre-existing turbulence, developed after the bow-shock crossing. Note that the full KHI time-series (magenta curves in Fig. 3) yields steeper magnetic spectra with the index near -1.8 in the inertial range.

In the ion range, both velocity and magnetic field show spectral indexes close to -3, except for the magnetic fluctuations in the MS, closer to -2.3. This is generally in agreement with previous observations. The Elsasser fields magnitude have slightly shallower spectral indexes, still included in the typical range between -2.2 and -2.7 (see Fig. 4). In the bottom panels of Fig. 4, the power spectra of ion density n, magnetic pressure $P_{\rm mag}$, and thermal pressure $P_{\rm th}$ are shown, normalized to the respective average value, for the BL (bottom left-hand panel) and MS (bottom right-hand panel) intervals. In the BL, spectral exponents in $f \in [0.04, 0.4]$ Hz are in turn $\alpha = -1.20, -1.35$, and -1.18, and in the high frequency range, $f \in [0.8, 2.5]$ Hz, $\alpha = -2.0, -2.42$, and -2.1. Note the sub-harmonics of the driving instability, visible in the magnetic pressure as distinct spectral bumps. In the MS, $\alpha = -1.67, -1.97$, and -1.94 for $0.04 < f < 0.3$ Hz. All spectra flatten in an intermediate range ($0.3 < f < 1.3$ Hz) where $\alpha = -1.20, -1.63$, and -1.56; further steepen is seen at higher frequencies. Uncertainty on the scaling exponents here is higher due to the narrowness of the frequency range.

In both MS and BL intervals, the turbulence is generally balanced, the two Elsasser variables have very similar statistics. The average normalized cross-helicity of fluctuations $\sigma_C = (\langle(\delta z^+)^2\rangle - \langle(\delta z^-)^2\rangle)/(\langle(\delta z^+)^2\rangle + \langle(\delta z^-)^2\rangle)$, where $\delta z^{\pm}$ is the fluctuation about the mean field, is small positive, around $\sigma_C = 0.075$ and $\sigma_C = 0.069$, for the BL and MS intervals, respectively. The scale-dependent cross-helicity obtained from increments correlation is shown in the top panel of Fig. 5. The BL displays positive values of cross helicity around $\sigma_C = 0.2$ throughout the inertial and ion scales; while in the MS an alternating sign is observed, and small positive values around $\sigma_C = 0.07$ are found at ion scales. Finally, the bottom panel of Fig. 5 shows the scale-dependent correlation between magnetic field magnitude and density,

$$\tilde{\rho}_{nB}(\tau) = \frac{\langle \Delta|\boldsymbol{B}| \cdot \Delta n\rangle}{(\langle \Delta|\boldsymbol{B}|^2\rangle \langle \Delta n^2\rangle)^{1/2}}, \quad (1)$$

where $\Delta n = n(t) - n(t+\tau)$, and $\Delta|\mathbf{B}| = |\mathbf{B}(t)| - |\mathbf{B}(t+\tau)|$. A strong anticorrelation is found at scales smaller than 2 s, which suggests that the thermal pressure (and so the density) is anticorrelated with the magnetic pressure, so that the fluctuations of total pressure are suppressed as previously observed, e.g. by Roberts et al. (1987). Note that $\tilde{\rho}(\tau)$ is equivalent to the one-point classic correlation between two high-pass filtered fields with scale τ. Note also that, while BL intervals are anticorrelated at all scales up to the driving, MS becomes positively correlated at $\tau \gtrsim 4$ s.

4 INTERMITTENCY

Turbulent fluctuations are usually characterized by intermittency, which in this case refers to the scale-dependent statistics of the field fluctuations. This is the signature of the concentration of the fluctuation energy in small regions of space, where scattered small-scale high-energetic structures are generated (Frisch 1995; Bruno & Carbone 2013). The standard diagnostics to describe the degree of intermittency include the scale-dependent probability density functions (PDFs) of the fluctuations or, equivalently, their moments, i.e. the structure functions.

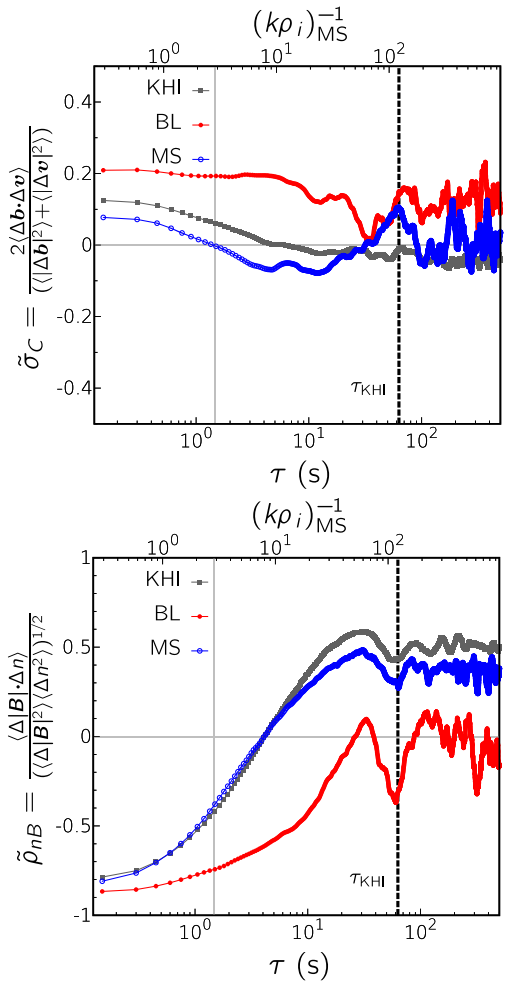

Figure 5. Top panel: the scale-dependent normalized cross helicity. Bottom panel: scale-dependent correlation between magnetic field magnitude and density, $\tilde{\rho}_{nB}$. In both panels, a grey vertical line indicates the ion inertial scale.

The scale-dependent q-th moments of the PDF of a field component f were computed as $S_q(\Delta t) = \langle \Delta f^q \rangle$ using the two ensembles of MS and BL intervals separately, for all components of velocity and magnetic field. The symbol $\langle \cdot \rangle$ indicates ensemble averages. The top left-hand panel of Fig. 6 shows an example of structure functions for the v_x component in the MS. Power-law fits $S_q \sim \Delta t^{\zeta_q}$, in a region roughly corresponding to the inertial range (as observed in the corresponding power spectra) are also represented in the same figure. The scaling exponents ζ_q are then collected and plotted in the bottom left-hand panel of Fig. 6. A similar analysis was performed for all the fields under study. In some occasions, when the scaling of higher order moments was not evident, Extended-self-similarity (ESS) has been used to obtain the scaling exponents (Benzi et al. 1993). The technique consists of fitting the power-law relation $S_q \sim S_3^{\xi_q}$, and using the fitted scaling of $S_3 \sim \Delta t^{\zeta_3}$ to recover the ζ_q exponents from the fitted ξ_qs. An example of ESS fit is shown in the top right-hand panel of Fig. 6 for the same case as in the top left-hand panel. A quantitative parametrization of intermittency could be achieved by modelling the anomalous scaling of the exponents, for example by fitting their order-q dependence to a p-model (Meneveau

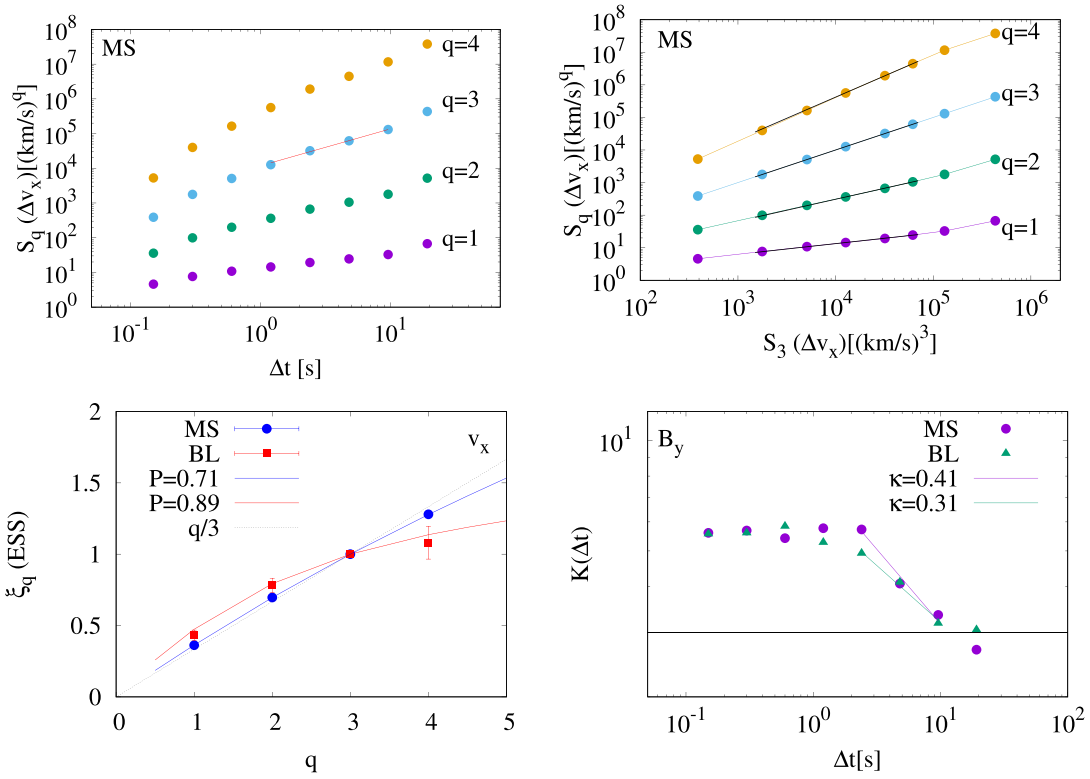

Figure 6. Top left-hand panel: scaling of the qth-order structure functions for the v_x component of the magnetosheath ion velocity. For the third order, a power-law fit is also shown. Top right-hand panel: the qth-order structure functions as a function of the third order structure function (ESS) for the v_x component of the magnetosheath ion velocity. Power-law fit are indicated. Bottom left-hand panel: the anomalous scaling exponents ξ_q as obtained for the v_x component. The dashed line is the linear prediction $\xi_q = q/3$, while the full lines are p-model fits. The resulting intermittency parameters p are indicated. Bottom right-hand panel: scale-dependent kurtosis for the magnetic field component B_y in both samples. Power-law fits $K \propto \Delta t^{-\kappa}$ are superposed in the inertial range, and the scaling exponents κ are indicated. The horizontal dotted line indicates the Gaussian value $K = 3$.

& Sreenivasan 1987). Such model predicts the order dependence of the scaling exponents $\zeta_q = 1 - \log_2[P^{qH} + (1 - P)^{qH}]$, where H is the Hurst exponent, related to the spectral index through $\alpha = 2H + 1$, or to the structure function scaling exponents through $\zeta_q = qH$, and it indicates the 'roughness' of the field. In this work, H has been estimated as $H = \zeta_3/3$. The fitting parameter $P \in [0.5, 1]$ is associated to intermittency, so that larger P corresponds to larger intermittency. The full lines in the bottom left-hand panel of Fig. 6 represent those fits, and the resulting intermittency parameters P are collected in Table 2. The model fits the data very well in all cases, but the value of the fitting parameter is affected by large error, making the quantitative estimate only approximate. Finally, the adimensional ratio between the fourth- and (squared) second-order structure functions $K = S_4/S_2^2$, called kurtosis, provides a measure of the scale-dependent 'flatness' of the PDF. Larger values of K are associated with higher tails, or larger deviation from the large-scale distribution (Gaussian in this case, for which $K = 3$). The kurtosis should scale as a power law of the time increment $K = \Delta t^{-\kappa}$, and the scaling exponent κ is related to the efficiency of the energy transfer mechanism in the cascade or, equivalently, to the shape and fractal dimension of the intermittent structures (Carbone & Sorriso-Valvo 2014). In the bottom right-hand panel of Fig. 6 an example of kurtosis scaling is shown for the B_y component in both samples. Power-law fits are indicated by full lines, and the scaling exponents for all cases are collected in Table 2. In the same table, the maximum values of kurtosis K_{max}, i.e. the maximum deviation from Gaussian of the fluctuations PDFs, are also indicated.

Table 2. Intermittency parameters estimated through the statistical analysis of the fields fluctuations, for both regions: the Hurst exponent H, the p-model intermittency parameter P, the scaling exponent of the kurtosis κ, and the maximum value of the kurtosis K_{max}.

		H	P	κ	K_{max}
MS	v_x	0.35 ± 0.01	0.71 ± 0.30	0.05 ± 0.02	4.6
	v_y	0.26 ± 0.04	0.65 ± 0.29	0.27 ± 0.08	4.4
	v_z	0.32 ± 0.02	0.77 ± 0.35	0.16 ± 0.03	4.6
	B_x	0.23 ± 0.02	0.68 ± 0.33	0.14 ± 0.06	4.5
	B_y	0.31 ± 0.02	0.59 ± 0.43	0.41 ± 0.06	5.8
	B_z	0.30 ± 0.01	0.51 ± 0.49	0.43 ± 0.50	9.9
BL	v_x	0.19 ± 0.05	0.89 ± 0.43	0.32 ± 0.05	4.8
	v_y	0.23 ± 0.02	0.72 ± 0.34	0.17 ± 0.09	4.8
	v_z	0.13 ± 0.07	0.62 ± 0.26	0.09 ± 0.10	4.3
	B_x	0.42 ± 0.01	0.65 ± 0.34	0.16 ± 0.08	5.0
	B_y	0.22 ± 0.01	0.68 ± 0.33	0.31 ± 0.03	5.8
	B_z	0.07 ± 0.07	0.75 ± 0.38	0.20 ± 0.03	5.1

According to the values of the parameter P and K_{max}, the overall intermittency level is low for most of the field components. Exceptions are observed for v_z in the MS, and v_x in the BL (larger P), and for B_z in the BL (larger K_{max}). However, error bars on the parameter P are too large to allow conclusive statements. Furthermore, the B_z fluctuations have smaller amplitude and shallower power-law scaling than their x and y counterparts, so that the small-scale structures will

immediately stick out and result in larger kurtosis. Note also that in the particular example presented in the figure, the BL samples (red) show a stronger intermittency than for the MS samples (blue), with a more evident deviation from linear scaling. However, the general behaviour is consistent with low intermittency in both regions, as can be observed looking at Table 2. Similar intermittency values were previously measured in the MS and in the magnetosphere (Echim M., Lamy & and Chang 2007; Macek et al. 2017). On the other hand, the large kurtosis scaling exponents κ (and in some occasions the values of P) are consistent with standard values observed in intermittent plasmas (Di Mare et al. 2019; Sorriso-Valvo et al. 2019b). This suggests that non-linear processes are actively and rapidly building up an intermittent energy cascade.

From the compared analysis of the spectral and intermittency properties, we can therefore conclude that, despite the presence of non-linear interactions building up intermittency, the very limited spectral range (and therefore the small associated Reynolds' number), the young stage of turbulence, and the effect of the KHI (resulting in the presence of several non-turbulent, small-scale structures acting as localized small-scale forcing, particularly seen in the BL, see Fig. 1) prevent the turbulence becoming fully developed and the kurtosis reaching large values expected for a standard turbulent flow, at least at this stage in the development of the KHI.

5 MHD AND HALL–MHD THIRD-ORDER SCALING LAWS OF TURBULENCE

Recent theoretical results on incompressible MHD and Hall–MHD turbulence have encouraged a more detailed study of the cascade by means of the scaling of the third-order moments of the fluctuating fields. Under the assumptions of homogeneity, isotropy, and large Reynolds number, the mean rate at which the energy is transferred across scales in the turbulent cascade obeys the Politano–Pouquet law (PP) (Politano & Pouquet 1998). When the Hall physics is included (Galtier 2008; Hellinger et al. 2018; Ferrand et al. 2019), such law reads:

$$-\frac{4}{3}\langle\varepsilon\rangle\Delta t\langle v\rangle = \langle|\Delta\boldsymbol{v}|^2\Delta v_L + |\Delta\boldsymbol{b}|^2\Delta v_L - 2(\Delta\boldsymbol{v}\cdot\Delta\boldsymbol{b})\Delta b_L + -\frac{d_p}{2}|\Delta\boldsymbol{b}|^2\Delta j_L + d_p(\Delta\boldsymbol{b}\cdot\Delta\boldsymbol{j})\Delta b_L\rangle. \quad (2)$$

Here $\langle\varepsilon\rangle$ indicates the mean energy transfer rate and $\boldsymbol{j}$ is the electric current. The subscript L indicates projection along the sampling direction $\langle\boldsymbol{v}\rangle/|\langle\boldsymbol{v}\rangle|$. The Hall Politano–Pouquet law (equation 2) quantifies the net transfer of energy towards small scales. This corresponds to the tiny imbalance between interactions acting to transfer energy from larger to smaller structures (direct transfer, e.g. through stretch and folding of vortexes, disruption of current filaments, and so on) and those acting in the opposite direction (inverse transfer, e.g. merging of structures, self-organization). Such imbalance is usually a small fraction of the whole transferred energy, so the observation of the PP law requires sensitive data analysis and appropriate statistical convergence. Furthermore, a well-developed turbulence (i.e. large Reynolds number) is required for the PP scaling to settle, so that its presence is a good estimator of the 'quality' of turbulence. Despite its ephemeral nature, the PP and Hall–PP laws have been broadly observed in numerical simulations (Sorriso-Valvo et al. 2002; Hellinger et al. 2018; Ferrand et al. 2019) and in space plasmas (MacBride et al. 2005; Sorriso-Valvo et al. 2007; Marino et al. 2008; Smith et al. 2009; Marino et al. 2012; Banerjee et al. 2016; Andrés et al. 2018; Hadid et al. 2018; Bandyopadhyay et al. 2020), and have provided important insight on the energy budget of solar wind turbulence. In this work, a comparison between the two regions is made in terms of the PP law. Further information is obtained by comparing the contribution of the different terms of equation (2), each representing specific features of the fluctuations and, consequently, specific energy transfer mechanisms or channels. More specifically, the first two terms of the right-hand side of equation (2), $Y_e = (|\Delta\boldsymbol{v}|^2 + |\Delta\boldsymbol{b}|^2)\Delta v_L$, represent the kinetic and magnetic fluctuation energy non-linearly coupled to the velocity structures (e.g. by vortexes), which is basically due to the fluid nature of the cascade. The third term, $Y_c = -2(\Delta\boldsymbol{v}\cdot\Delta\boldsymbol{b})\Delta b_L$, accounts for the reduction of the non-linear interactions by the decorrelation effect associated with the presence of coupled 'Alfvénic' velocity–magnetic fluctuations non-linearly interacting with the magnetic structures (e.g. current sheets or tangential discontinuities) (Dobrowolny, Mangeney & Veltri 1980). These three terms together represent cross-scale transfer of energy through fluid mechanisms $Y = Y_e + Y_c$. The last two terms are the Hall contribution to the energy transfer. In particular, $H_1 = -d_p|\Delta\boldsymbol{b}|^2\Delta j_L/2$ accounts for the magnetic energy transported by the electric current in the flow direction, while $H_2 = d_p(\Delta\boldsymbol{b}\cdot\Delta\boldsymbol{j})\Delta b_L$ represents the fluctuations-related current helicity transported by the magnetic fluctuations, so that $H = H_1 + H_2$ is the overall Hall contribution.

While each term of equation (2) provides energy transfer independent of the other terms, the PP law only predicts that the combination of all terms is a linear function of the scale. This is particularly evident in Fig. 7, where the scaling laws and their different contributions are plotted for the two regions, in both MHD and Hall–MHD versions. In all panels of this figure, open symbols indicate negative values of the moment, and are plotted in absolute value in order to allow their display with logarithmic axes. In the top left-hand panel, the MHD version of the PP law is shown for the MS (blue) and BL (red) samples. A linear scaling is suggested in the BL, while the linear dependence is less evident in the MS. A linear fit in the inertial range (not shown) provides $\langle\varepsilon_{BL}\rangle = 60 \pm 11\,\mathrm{MJkg^{-1}s^{-1}}$ and $\langle\varepsilon_{\mathrm{MS}}\rangle = 1.2 \pm 0.3\,\mathrm{MJkg^{-1}s^{-1}}$ for the two regions. These values are consistent with the cascade rates found by Franci et al. (2020) within the KH vortices without dividing them up into MS and BL sub-regions, and suggest that the BL turbulent energy transfer rate is one order of magnitude larger than in the MS. Such observation should be combined with the evidence that the third-order moment linear scaling is more evident in the BL than in the MS. Hence, while order of magnitude estimates and the observation of the spectra and kurtosis scaling suggest a similar turbulence in the two regions, the third-order moment reveals some substantial difference in the effectiveness of the non-linear interactions. A look at the bottom panels of Fig. 7 also shows that the MS scaling is not supported by regular, steady contribution from all scales. Several changes of sign and lack of scaling of the individual components result in cancellation of energy transfer, with consequent reduction of both the global scaling quality and amplitude. This may be enhanced by kinetic effects taking place in the MS, due to different competing mechanisms at and around the proton scales.

When including the Hall terms (top right-hand panel) the linear scaling is completely lost, and several sign changes are observed in both regions. The reason for this is evident in the bottom panels, which show the breakdown of the PP law in terms of their components (coloured markers) in the Hall–MHD case. As can be seen, the Hall contributions are large and irregular, disrupting the linear scaling of the third-order moment. This observation seems to suggest that Hall-physics effects are largely present in both regions, and may possibly not be related to the turbulent cascade, in agreement with the spectral and intermittency analysis. However, caution should be

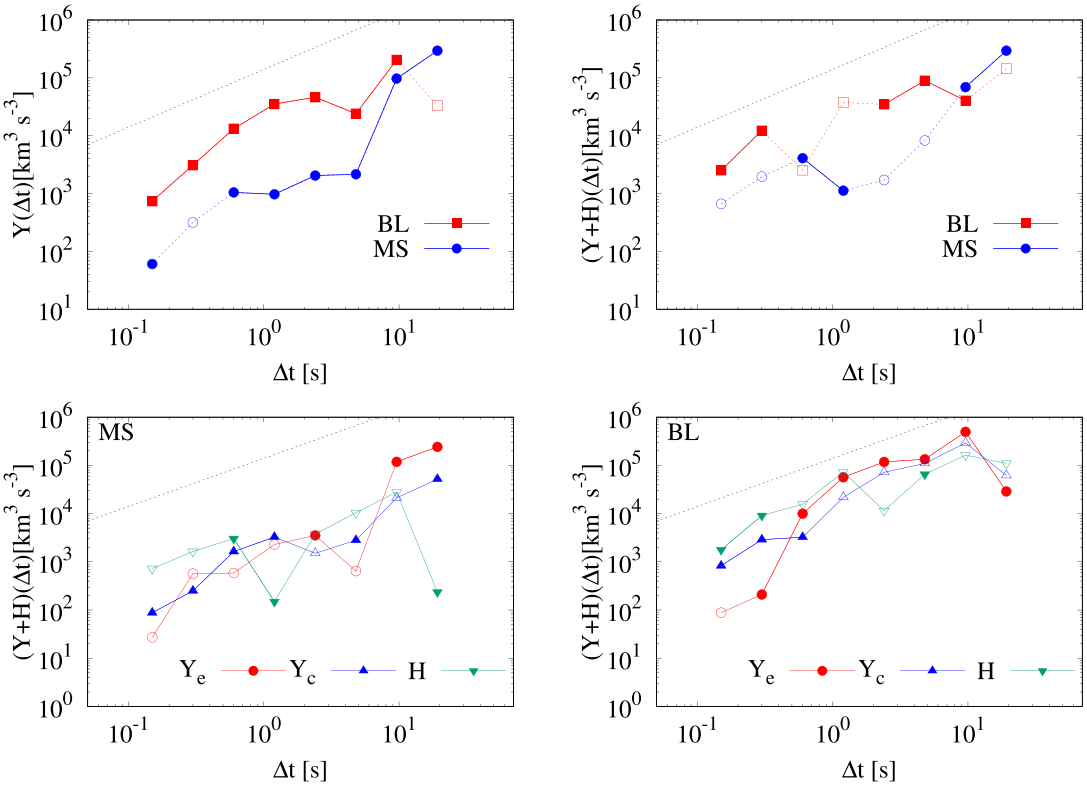

Figure 7. Top row: the Politano–Pouquet law for the magnetosheath (blue) and magnetospheric boundary layer (red) subsets, in the simple MHD version (left-hand panel) and in the extended Hall–MHD version (right-hand panel). Bottom panels: detail of the different contributions Y_e, Y_c, and H to the Hall–Politano–Pouquet law for the magnetosheath (left-hand panel) and boundary layer (right-hand panel) subset.

used in interpreting the global scaling laws. Indeed, the data set used for the statistics may not be sufficiently large as to allow convergence of the third-order moment, in particular in its Hall–MHD version.

6 MHD AND HALL–MHD LOCAL ENERGY TRANSFER PROXY: STATISTICAL PROPERTIES

Finally, the properties of the turbulent cascade can be studied using a proxy of the local energy transfer rate (LET), which gives an indication of the contribution of the fluctuations to the energy cross-scale flux at each position (or, as in this case at each time in the time-series through the Taylor hypothesis). The LET is simply introduced as the unaveraged argument of the Politano–Pouquet law, equation (2), namely:

$$\varepsilon = -\frac{3}{4\langle v\rangle\Delta t}\left[|\Delta\boldsymbol{v}|^2\Delta v_L + |\Delta\boldsymbol{b}|^2\Delta v_L - 2(\Delta\boldsymbol{v}\cdot\Delta\boldsymbol{b})\Delta b_L\right] + \frac{3}{4\langle v\rangle\Delta t}\left[\frac{d_p}{2}|\Delta\boldsymbol{b}|^2\Delta j_L - d_p(\Delta\boldsymbol{b}\cdot\Delta\boldsymbol{j})\Delta b_L\right], \quad (3)$$

where $\varepsilon \equiv \varepsilon(t, \Delta t)$ depends on both time and scale, and all the left-hand terms have been described in the previous section. An example of LET is shown in the two bottom panels of Fig. 1, respectively including and excluding the Hall terms from the sum in equation (3). The irregular, highly intermittent behaviour of the parameter is evident. While there are exact approaches to the local energy transfer rate estimators, mostly based on filtering techniques (Eyink & Sreenivasan 2006; Camporeale et al. 2018; Coburn & Sorriso-Valvo 2019; Kuzzay, Alexandrova & Matteini 2019), the local proxy introduced above provides useful information on the contribution to the energy flux from a specific position. It therefore represents an indicator of presence of 'non-linear activity', similar to other simpler indicators (e.g. the local intermittency measure (Farge et al. 1992) or the partial variance of increments (Greco et al. 2009)), but carrying additional information on the nature of the fluctuations: current or vorticity structures, correlated fluctuations, or Hall currents. It is therefore useful in order to examine the statistical properties of the LET in the different regions, for all different components, and at various scales. This can be done for example by estimating the scale-dependent probability distribution functions of ε and of its components. These will show presence of heavy tails, increasingly populated by strong intermittent structures as the non-linear interactions concentrate energy on small-scales. Examples of such distributions are shown in the four panels of Fig. 8, for the BL (top row) and MS (bottom rows) samples. Left-hand panels refer to the MHD version of the LET, while right-hand panels include the Hall contributions. PDFs referring to three different scales are shown in each plot. As expected, the shape of the distributions changes with the scale, in agreement with the LET parameter being associated with the intermittent structures, and illustrating the formation of small-scale, intermittent intense non-linear energy transfer regions. Note that the PDFs only refer to positive values $\varepsilon_{>0}$. Similar results were obtained separately for the negative tails of the distribution (not shown). Note that, looking at the PDFs of the LET proxy (whose average defines the third-order scaling law), it appears evident that in the BL the tails are higher than in the MS. This implies the presence of larger contributions to the Yaglom scaling, possibly resulting in the large difference in the energy transfer rate between the two regions.

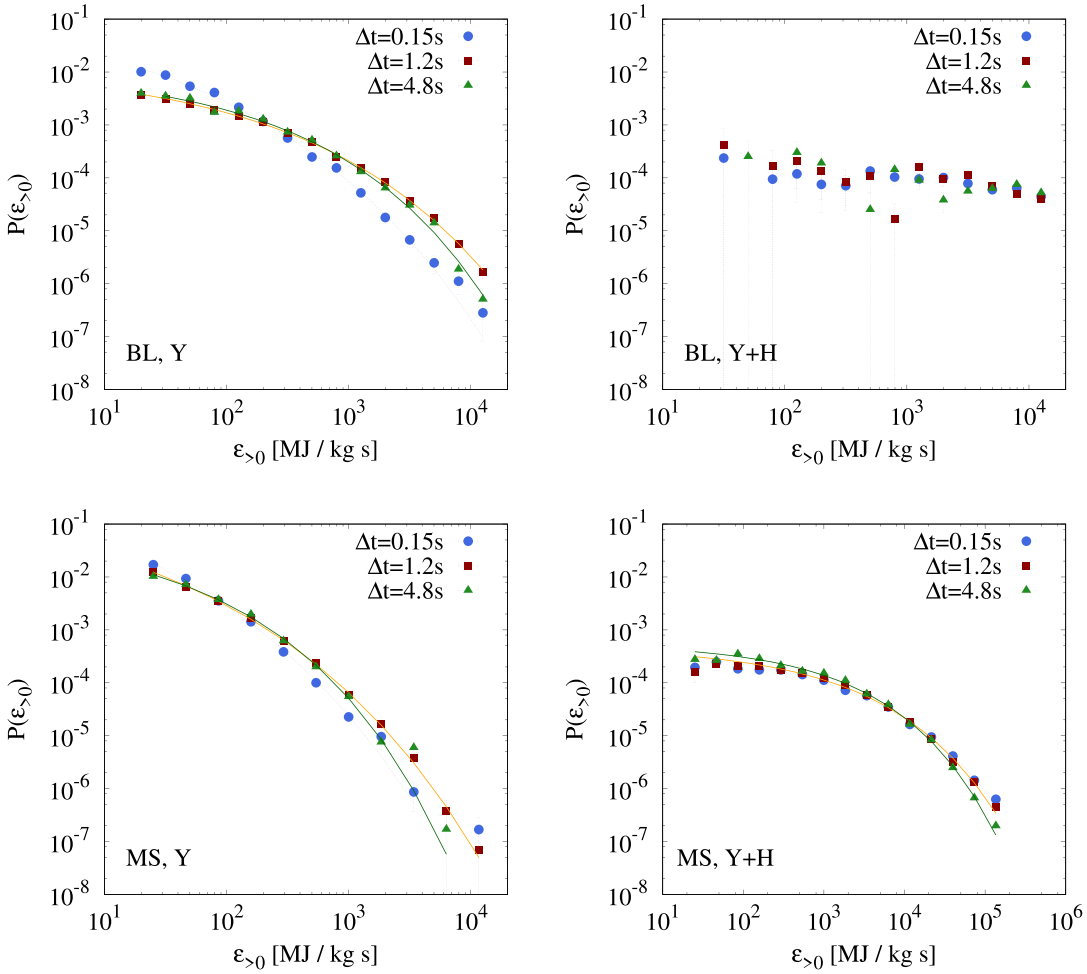

Figure 8. Distribution functions of the positive MHD local energy transfer proxy LET (Y, top left-hand panel) and Hall–MHD LET (Y+H, top right-hand panel) for the BL (top panels) and for the MS (bottom panels), estimated using the increments at the three indicated scales. In both samples for the MHD case, and in the MS only for the Hall–MHD case, a stretched exponential fit is superposed to the data (full lines).

The scaling invariance of the turbulent dynamics usually translates into the power-law scaling of some modelling parameters. It is therefore interesting to fit the data to a model and examine the scaling properties of the resulting parameters. Within the standard picture of multifractal turbulence, the local energy transfer at a given scale and position can be imagined as the result of a multiplicative cascade of random factors, each representing the fraction of energy transferred by non-linear interaction across pairs of adjacent larger scales. At the smallest scales of the cascade, the LET can be ideally associated to the local energy dissipation rate in an ordinary turbulent flow. Energy transfer and dissipation rates can be modelled, for example, in the framework of the extreme deviation theory (EDT), a popular description in which the statistics of a fluctuating quantity resulting from a multiplicative cascade is controlled by few extreme events (Frisch & Sornette 1997). This applies to turbulence, where the small-scale statistics are dominated by a few intense intermittent structures. EDT predicts stretched exponential distributions $P(\varepsilon) \sim e^{-b|\varepsilon|^c}$ of the energy transfer and dissipation rates. The scale-dependent parameter c controls the shape of the distribution. In particular, $c = 2$ describes a Gaussian distribution, typically observed for the turbulent energy transfer at large scales; $c = 1$ an exponential distribution; and values $c < 1$ are associated with increasingly high-tailed distributions, typical of small-scale intermittent dissipation. The variation of the parameter across scales, and in particular the presence of power-law scaling, is therefore indicative of the PDF modification occurring because of intermittency. Similar to the fluctuation's kurtosis scaling exponent κ, the power-law exponent c carries additional information on the efficiency of the cascade, i.e. on the number of non-linear interactions necessary to carry the energy to the smallest scales. In this sense, steeper power laws will be indicative of faster cascades, usually associated to smaller fractal dimension (or space filling factor) of the intermittent structures.

In Fig. 8, stretched exponential fits of the LET distributions are indicated as full lines. All of the MHD terms were modelled successfully (left-hand panels), while the Hall terms were only following a stretched exponential distribution in the MS (bottom right-hand panel). In the case of the BL, the distributions of the Hall contributions (not shown), and therefore of the total Hall LET (top right-hand panel), are quite irregular and relatively flat at all scales, indicating substantial presence of large fluctuations and lack of general scaling properties. Once again, this confirms that the origin of the strong Hall currents and magnetic structures should not be ascribed to a developed turbulent cascade, particularly in the BL.

To conclude the analysis, Fig. 9 shows the scaling behaviour of the stretched exponential fitting parameter of the LET distribution functions c, separately for the three different MHD components,

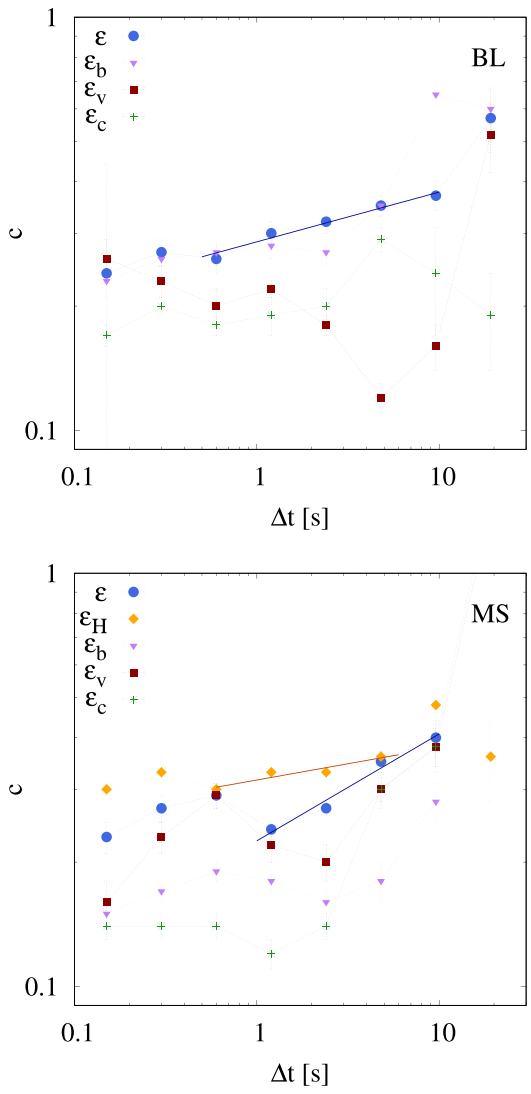

Figure 9. Scaling parameter c as obtained from the fit of the LET distribution functions for the different contributions and for the total, in the boundary layer (top panel) and in the magnetosheath (bottom panel). The full lines represent power-law fits $c \propto \Delta t^{\gamma}$ with scaling exponent for the MHD LET $\gamma_{\rm BL} = 0.12 \pm 0.01$, $\gamma_{\rm MS} = 0.26 \pm 0.03$. In the MS case, the scaling exponent for the complete Hall–MHD LET is $\gamma_{\rm MS-H} = 0.08 \pm 0.02$.

indicated here as ε_v, ε_b, and ε_c, and for the total MHD and Hall–MHD estimates, ε and ε_H. As noted above, power-law scaling of c is expected for a quantity that describes a turbulent cascade, such as the LET. The various partial contributions do not show particular scaling behaviour. This is not surprising, since the Politano–Pouquet law only predicts scaling properties for the full mixed third-order moment. On the contrary, the total MHD proxy ε clearly displays a power-law scaling $c \propto \Delta t^{\gamma}$ in the BL samples, with $\gamma_{\rm BL} = 0.12 \pm 0.01$, and in the MS samples, with $\gamma_{\rm MS} = 0.26 \pm 0.03$. This indicates that once again the proxy correctly captures the scaling properties of the turbulent cascade, in agreement with the Politano–Pouquet law. In the MS case, the Hall–MHD LET parameter also show scaling properties, with a less efficient exponent $\gamma_{\rm MS-H} = 0.08 \pm 0.02$, indicating that, at least in the MS, the nature of the magnetic and current fluctuations could be originating from a turbulent cascade, perhaps not yet visible in the global scaling. Note that in the BL case the global scaling exponent is compatible with the value previously observed in the inner heliosphere using Helios 2 data ($\gamma = 0.09 \pm 0.02$) (Sorriso-Valvo et al. 2018), suggesting a possible common efficiency of the non-linear interactions. The MS energy transfer has a shorter scaling range, but larger exponent, indicating a faster cascade rapidly generating small-scale structures. This interesting difference could be explained considering the stronger contribution of the cross-helicity terms inhibiting the cascade in the BL, and the additional contribution from the Hall terms in the MS, both of which can be seen in the two panels of Fig. 9. The study of the LET therefore highlights differences between the two regions, additional with respect to those observed using the results from spectral and intermittency analysis, and provides information about the nature of the fluctuations and the efficiency of the non-linear interactions that generate the turbulence.

7 CONCLUSIONS

The recent measurements collected by the MMS satellites have provided great insight on the properties of plasma in various magnetospheric regions. Among these, in several occasions MMS has sampled plasma and fields across the magnetopause, separating the quieter magnetospheric boundary layer from the faster flowing magnetosheath. On 2015 September 8, MMS crossed one such structures longitudinally, providing a long sample of alternating MS and BL regions in the early phase of the KH mixing. This provided an occasion to characterize and compare the properties of turbulence on both sides of the magnetopause. To this aim, we have accurately selected various sub-intervals from each of the two regions, and studied the statistical properties of the fluctuations. Power spectra, intermittency properties, and the global and local third-order moment scaling have been studied here. It is worth highlighting that the excellent performance of the compressed sensing technique, used here to evaluate the power spectral density for the two discontinuous samples, has allowed the identification of the KHI period as an evident peak in the spectra of various quantities.

The spectral analysis suggested a similar presence of turbulent fluctuations in the two regions, although the BL has less defined spectral scaling and shallower spectra for all field components. On the other hand, intermittency results did not show significant differences between the two regions. Moreover, there is an indication of developing cascade due to strong non-linear interactions, but not yet fully established as to generate strong intermittency.

The global third-order moment scaling, studied through the MHD and Hall–MHD Politano–Pouquet relations, revealed the presence of proper scaling only for the MHD version. The energy transfer rate in the BL was one order of magnitude larger than in the MS, pointing at some substantial difference in the effectiveness of the non-linear interactions or in the development stage of the turbulence. The observed difference indicates that in the BL the non-linear interactions are more effectively forming a turbulent cascade (starting from the absence of power-law spectra typical of that region) through more ordered and stronger contributions from local fluctuations. This is not in contrast with spectral and intermittency quantities, which provide information on different aspects of the turbulence. The observed difference is therefore not only relevant, but also an important new result, indicating a more effective onset of turbulence in the BL with respect to the MS.

Including the Hall terms to the global scaling results in the disruption of the scaling law, due to the large value and highly variable sign of those terms, whose contribution to the cascade may not have fully settled or could be corrupted by kinetic plasma physical processes not accounted for in the PP law.

Finally, the probability density functions of the local proxy were successfully modelled to a stretched exponential function, typical of dissipation-like quantities. The scaling properties of the fitting shape parameter were used to assess the existence of an effective cascade mechanism. Power-law scaling relations were indeed observed for the local proxy of the total MHD energy transfer rate in both regions, while single-contribution terms did not show any scaling. However, adding Hall terms again disrupted the scaling of the fitting parameter in the BL samples, supporting the scenario where the presence of large Hall fluctuations, associated with strong intermittency, is not necessarily associated to a non-linear cascading process, but may be instead of different nature. On the contrary, the MS samples showed approximate scaling also for the Hall–MHD proxy, indicating that a Hall–MHD cascade may be at work, although it is not developed enough as to provide sign-definite contributions to the global scaling.

This behaviour of the Hall–MHD terms could potentially result from a number of features of the physical system. The system may be in a transient, early stage in the development of the turbulence. Relative to idealized full particle-in-cell simulations of the 2015 September 8 Kelvin–Helmholtz event (Nakamura et al. 2017a, b), which indicate that the overall instability is in the early non-linear stage of development, the turbulence within the vortices appears to be more fully developed than expected. Recent numerical simulations have suggested that the onset of turbulence within the vortices may be enhanced due to the impact of preexisting turbulent fluctuations within the magnetosheath, which could both be entrained within the vortices and potentially help to seed secondary instabilities (Nakamura et al. 2020). The more detailed statistical analyses performed in this study may be teasing out subtle features indicating that, while the turbulence is perhaps more developed than expected, it is still in the process of reaching its fully developed state. Furthermore, the KH vortices form a complex boundary region within the magnetosphere and, therefore, may exhibit additional dynamics that go beyond purely homogeneous fluid turbulence. Notably, the mixing of the boundary layer and magnetosheath plasma populations within the vortices can lead to complex particle distribution functions and kinetic instabilities. Such behaviour has been noted in particular through the examination of high-frequency electric field activity in the 2015 September 8 KHI (Wilder et al. 2016, 2020). Vortex-induced reconnection events are also known to be set up by the large-scale configuration of the system, both at mid-latitudes associated with twisted field lines above and below the KH vortices and at the compressed current sheets between the vortices (e.g. Nykyri & Otto 2001; Faganello et al. 2012; Nakamura et al. 2013; Eriksson et al. 2016a; Vernisse et al. 2016). Effects such as these could perhaps influence the currents within the system, which could alter the behaviour of the Hall terms in particular. In fact, as observed by Stawarz et al. (2016), there appears to be enhanced electron velocity, and thus current, fluctuations, in particular in the component along the average magnetic field, within the event.

In conclusion, similarities and differences between the two adjacent regions were extensively presented. The overall result is that the two regions are characterized by different levels and 'cleaniness' of turbulence, presenting fluctuations that obey scaling laws to different degrees, as highlighted through various diagnostic quantities. In particular, the boundary layer plasma includes small-scale current structures that do not seem to proceed from the turbulent cascade, but may rather be of external origin, possibly related to the KHI. It would be interesting to have access to data in a more advanced stage of the KHI, where the mixing has occurred and the turbulence may have had the time to develop more completely. This work, subject to the availability of data, is left for future investigation.

ACKNOWLEDGEMENTS

PQ, CLV, and LSV were supported by Escuela Politecnica nacional (EPN) Internal Project PII-DFIS-2019-01. CLV was partially supported by EPN Internal Project PIM-19-01. LSV and EY were funded by the Swedish Contingency Agency, grant 2016-2102. LSV was supported by Swedish National Space Agency (SNSA) grant 86/20. FF was supported by National Aeronautics and Space Administration (NASA) grant 80NSSC19K0260. JES was supported by the Royal Society University Research Fellowship URF\R1\201286 and UKRI/STFC grant ST/S000364/1 during this project. RM acknowledges support from the project 'EVENTFUL' (ANR-20-CE30-0011), funded by the French 'Agence nationale de la recherche' – ANR through the program AAPG-2020.

DATA AVAILABILITY

MMS data are publicly available through the MMS Science Data Center (https://lasp.colorado.edu/mms/sdc/public).

REFERENCES

Alexandrova O., Carbone V., Veltri P., Sorriso-Valvo L., 2008, ApJ, 674, 1153
Andrés N., Sahraoui F., Galtier S., Hadid L. Z., 2018, J. Plasma Phys., 84, 905840404
Bandyopadhyay R. et al., 2020, Phys. Rev. Lett., 124, 225101
Banerjee S., Hadid L. Z., Sahraoui F., Galtier S., 2016, ApJ, 829, L27
Bavassano Cattaneo M. B. et al., 2010, Ann. Geophys., 28, 893
Benzi R., Ciliberto S., Tripiccione R., Baudet C., Massaioli F., Succi S., 1993, Phys. Rev. E, 48, R29(R)
Biskamp D., 1993, Nonlinear Magnetohydrodynamics, (Cambridge Monographs on Plasma Physics). Cambridge Univ. Press, Cambridge, UK
Breuillard H. L. et al., 2018, ApJ, 859, 127
Bruno R., Carbone V., 2013, Living Rev. Sol. Phys., 10, 2
Burch J. L. et al., 2016, Science, 352, aaf2939
Camporeale E., Sorriso-Valvo L., Califano F., Retinò A., 2018, Phys. Rev. Lett., 120, 125101
Candes, Romberg, Tao, 2006, Commun. Pure Appl. Math., 59, 1207
Carbone F., Sorriso-Valvo L., 2014, Eur. J. Phys. E, 37, 61
Chandran B. D. G., 2005, Phys. Rev. Lett., 95, 265004
Chen S. H., Kivelson M. G., 1993, Geophys. Res. Lett., 20, 2699
Chen S. H., Kivelson M. G., Gosling J. T., Walker R. J., Lazarus A. J., 1993, J. Geophys. Res., 98, 5727
Cho J., Lazarian A., Vishniac E. T., 2003, in Falgarone E., Passot T., eds, MHD Turbulence: Scaling Laws and Astrophysical Implications. Turbulence and Magnetic Fields in Astrophysics. Lecture Notes in Physics, Vol. 614. Springer, Berlin, Heidelberg
Coburn J. T., Sorriso-Valvo L., 2019, Fluids, 4, 163
Di Mare F., Sorriso-Valvo L., Retinò A., Malara F., Hasegawa H., 2019, Atmosphere, 10, 561
Dobrowolny M., Mangeney A., Veltri P., 1980, Phys. Rev. Lett., 45, 144
Donoho D. L., 2006, IEEE T. Inform. Theory, 52, 1289
Echim M. M., Lamy H., Chang T., 2007, Nonlinear Process. Geophys., 14, 525
Eriksson S. et al., 2016a, Geophys. Res. Lett., 43, 5606
Eriksson S. et al., 2016b, Phys. Rev. Lett., 117, 015001
Eyink G. L., Sreenivasan K. R., 2006, Rev. Modern Phys., 78, 87
Faganello M., Califano F., Pegoraro F., Andreussi T., Benkadda S., 2012, Plasma Phys. Control. Fusion, 54, 124037
Fairfield D. H. et al., 2000, J. Geophys. Res., 105, 21159
Fairfield D. H., Fairfield, Farrugia C. J., Mukai T., Nagai T., Federov A., 2003, J. Geophys. Res., 108, A12
Fairfield D. H., Kuznetsova M. M., Mukai T., Nagai T., Gombosi T. I., Ridley A. J., 2007, J. Geophys. Res., 112, A08206
Farge M., 1992, Annu. Rev. Fluid Mech., 24, 395
Farrugia C. J., Gratton F. T., Torbert R. B., 2001, Space Sci. Rev., 95, 443

Ferrand R. S. Galtier L., Sahraoui F., Meyrand R., Andrés N., Banerjee S., 2019, ApJ, 881, 50
Franci L. et al., 2020, ApJ, 898, 175
Fraternale F., Pogorelov N. V., Richardson J. D., Tordella D., 2019a, ApJ, 872, 40
Fraternale F., Pogorelov N. V., Richardson J. D., Tordella D., 2019b, 012006
Fraternale F., Pogorelov N. V., Burlaga L. F., 2020, ApJ, 897, L28
Frisch U., 1995, Turbulence: the legacy of A. N. Kolmogorov. Cambridge Univ. Press, Cambridge, UK
Frisch U., Sornette D., 1997, J. Phys. I, 7, 1155
Fujimoto M., Tonooka T., Mukai T., 2003, in Newell P. T., Onsager T., eds, Geophys. Monogr. Ser., AGU, Washington, DC, p. 133
Gallana L. et al., 2016, J. Geophys. Res., 121, 3905
Galtier S., 2008, Phys. Rev. E, 77, 015302(R)
Greco A., Matthaeus W. H., Servidio S., Dmitruk P., 2009, Phys. Rev. E, 80, 046401
Hadid L. Z., Sahraoui F., Galtier S., Huang S. Y., 2018, Phys. Rev. Lett., 120, 055102
Hasegawa H., Fujimoto M., Phan T. D., Reme H., Balogh A., Dunlop M. W., Hashimoto C., TanDokoro R., 2004, Nature, 430, 755
Hasegawa et al., 2019, J. Geophys. Res., 125, e2019JA027595
Hellinger P., Verdini A., Landi S., Franci L., Matteini L., 2018, ApJ, 857, L19
Huang S. Y., Hadid L. Z., Sahraoui F., Yuan Z. G., Deng X. H., 2017, ApJ, 836, L10
Johnson J. R., Wing S., Delamere P. A., 2014, Space Sci. Rev., 184, 1
Karimabadi H. et al., 2013, Phys. Plasmas, 20, 012303
Kokubun S., Yamamoto T., Acuna M. H., Hayashi K., Shiokawa K., Kawano H., 1994, J. Geomagn. Geoelectr., 46
Kuzzay D., Alexandrova O., Matteini L., 2019, Phys. Rev. E, 99, 053202
Lu S. W. et al., 2019, ApJ, 875, 57
Lui A. T. Y., Meneveau C., Sreenivasan K. R., 1987, Phys. Rev. Lett., 59, 1424
MacBride B. T., Forman M. A., Smith C. W., 2005, in Fleck B., Zurbuchen T. H., Lacoste H., eds, Proceedings of Solar Wind 11/SOHO 16, Connecting Sun, Heliosphere, (European Space Agency), Vol. 592, p. 613 Availabl e at: https://ui.adsabs.harvard.edu/abs/2005ESASP.592..613M
Macek W. M., Wawrzaszek A., Kucharuk B., Sibeck D. G., 2017, ApJ, 851, L42
Macek W. M., Krasińska A., Silveira M. V. D., Sibeck D. G., Wawrzaszek A., Burch J. L., Russell C. T., 2018, ApJ, 864, L29
Marino R., Sorriso-Valvo L., Carbone V., Noullez A., Bruno R., Bavassano B., 2008, ApJ, 677, L71
Marino R., Sorriso-Valvo L., D'Amicis R., Carbone V., Bruno R., Veltri P., 2012, ApJ, 750, 41
Mitchell D. G., Kutchko F., Williams D. J., Eastman T. E., Frank L. A., Russell C. T., 1987, J. Geophys. Res., 92(A7), 7394
Nakamura T. K. M., Daughton W., Karimabadi H., Eriksson S., 2013, J. Geophys. Res., 118, 5742
Nakamura T. K. M., Hasegawa H., Daughton W., Eriksson S., Li W. Y., Nakamura R., 2017a, Nat. Commun., 8, 1582
Nakamura T. K. M., Eriksson S., Hasegawa H., Zenitani S., Li W. Y., Genestreti K. J., Nakamura R., Daughton W., 2017b, J. Geophys. Res., 122, 11505
Nakamura T. K. M., Stawarz J. E., Hasegawa H., Narita Y., Franci L., Wilder F. D., Nakamura R., Nystrom W. D., 2020, J. Geophys. Res., 125, e27515
Nykyri K., Otto A., 2001, Geophys. Res. Lett., 28, 3565
Otto A., Fairfield D. H., 2000, J. Geophys. Res., 105, 21
Perri S. et al., 2020, J. Plasma Phys., 86, 905860108
Petrovay K., 2001, Space Sci. Rev., 95, 9
Politano H., Pouquet A., 1998, Geophys. Res. Lett., 25, 273
Pollock C. et al., 2016, Space Sci. Rev., 199, 331
Pucci F., Malara F., Perri S., Zimbardo G., Sorriso-Valvo L., Valentini F., 2016, MNRAS, 459, 3395
Roberts D. A., Klein W., Goldstein M. L., Matthaeus W. H., 1987, J. Geophys. Res., 92, A10
Russell C. T. et al., 2016, Space Sci. Rev., 199, 189
Saur J., Politano H., Pouquet A., Matthaeus W. H., 2002, A&A, 386, 699
Smith C. W., Stawarz J. E., Vasquez B. J., Forman M. A., MacBride B. T., 2009, Phys. Rev. Lett., 103, 201101
Sorriso-Valvo L., Carbone V., Noullez A., Politano H., Pouquet A., Veltri P., 2002, Phys. Plasmas, 9, 89
Sorriso-Valvo L. et al., 2007, Phys. Rev. Lett., 99, 115001
Sorriso-Valvo L., Carbone F., Perri S., Greco A., Marino R., Bruno R., 2018, Sol. Phys., 293, 10
Sorriso-Valvo L. et al., 2019, Phys. Rev. Lett., 122, 035102
Sorriso-Valvo L. et al., 2019, Front. Phys., 7, 108
Stawarz J. E. et al., 2016, J. Geophys. Res. Space Phys., 121, 11021
Stawarz J. E. et al., 2019, ApJ, 877, L37
Sundberg T., Boardsen S. A., Slavin J. A., Anderson B. J., Korth H., Zurbuchen T. H., Raines J. M., Solomon S. C., 2012, J. Geophys. Res., 117, A04216
Treumann R. A., 1999, Adv. Space Res., 24, 3
Uritsky V. M, Paczuski M., Davila J. M., Jones S. I., 2007, Phys. Rev. Lett., 99, 025001
Vernisse Y. et al., 2016, J. Geophys. Res., 121, 9926
Von Papen M., Saur J., Alexandrova O., 2014, J. Geophys. Res., 119, 2797
Vörös Z., Yordanova E., Echim M. M., Consolini G., Narita Y., 2016, ApJ, 819, L15
Wilder F. D. et al., 2016, Geophys. Res. Lett., 43, 8859
Wilder F. D. et al., 2020, Geophys. Res. Lett., 47, e87837
Yordanova E. et al., 2016, Geophys. Res. Lett., 43, 5969
Yordanova E., Vörös Z., Raptis S., Karlsson T., 2020, Front. Astron. Space Sci., 7, 2
Zimbardo G., Greco A., Veltri P., Voros Z., Taktakishvili A. L., 2008, Astrophys. Space Sci. Trans., 4, 35

This paper has been typeset from a TEX/LATEX file prepared by the author.